Automatic Target Recognition via the Simulation of Infrared Scenes

Aaron D. Lanterman, Michael I. Miller, Donald L. Snyder
Electronic Systems and Signals Research Laboratory
Department of Electrical Engineering
Washington University
Campus Box 1161
Washington University
St. Louis, Missouri 63130-4899

ABSTRACT

Many FLIR simulation efforts have been undertaken with the goals of training and testing automatic target recognition algorithms and predicting performance. In our pattern theoretic Grenander/Bayesian approach to the ATR problem, simulation provides the heart of the ATR algorithm itself. An hypothesized scene, simulated from the emissive characteristics of the hypothesized scene elements, is compared with the collected data by a likelihood function based on sensor statistics. This likelihood is combined with a prior distribution defined over the set of possible scenes to form a posterior distribution. Jump-diffusion processes which sample from the posterior provide the engine of the inference algorithm. New objects are detected and object types are recognized through discrete jump moves. Between jumps, the location and orientation of objects are estimated via continuous diffusions.

Both the diffusion and jump operations involve the simulation of scenes produced by hypothesized configurations. The radiant intensities of ground vehicles are simulated with Keweenaw Research Center's PRISM code. Rendering the scene is most effectively accomplished by pipelined rendering engines such as Silicon Graphics. We demonstrate the execution of our algorithm on a Silicon Graphics Onyx/Reality Engine.

1 INTRODUCTION

Automatic target recognition (ATR) systems may encounter a wide spectrum of scenarios, characterized by three fundamental difficulties: 1) *Geometric variability:* Targets may take on different appearances depending on the orientations and positions of the object; 2) *Image variability:* The data obtained may vary with environmental conditions and will be subject to the noise characteristics of the sensor. In addition, the textures comprising a scene will have randomness associated with them since it is not feasible to specify every minute aspect of a scene; 3) *Complexity/scene variability:* The number of targets encountered will not be known in advance, and targets may enter or leave the scene at random times. The development of ATR systems invariant to all three kinds of variability depends upon a framework for the understanding and representation of complex real and natural scenes. Grenander's *general pattern theory* [1, 2] offers this essential infrastructure for the representation and inference of structures in complex systems [3].

Although this work focuses on the development of a pattern theoretic algorithm for a forward-looking infrared sensor mounted on an airborne platform [4, 5, 6], the principles employed are not particular to FLIR sensors. To illustrate the generality of our framework, we also present a model for a LADAR sensor which may be used instead of or in addition to our FLIR model.

1.1 Pattern Theory for ATR

Tremendous effort has gone into the development of ATR algorithms. The more sophisticated "model-based" systems classify based on CAD-like models [7, 8]. Traditional algorithms maintain a conceptual separation between "low-level" vision (edge detection, segmentation, etc.) and higher levels of inference (classification.)

Our "top-down" pattern theoretic philosophy represents a dramatic departure from traditional machine vision al-

gorithms. Instead of performing separate steps of segmentation, feature extraction, etc., our approach *estimates the configuration of targets directly from the measured data.* Patterns, such as those known by an automatic target recognition system, are represented as templates. These templates are subjected to transformations forming *mathematical groups*, and the transformations which yield a best match to the measured data are chosen as the solution. Thus, our ability to *recognize* pattern depends directly on our ability to *synthesize* those patterns. Our work has been guided by this paradigm of *recognition through simulation.*

We take a Bayesian approach in which a hypothesized scene, simulated from the emissive characteristics of the hypothesized scene elements, is compared with the collected data by a likelihood function based on sensor statistics. Thus, simulation technology is central to our work in two distinct ways: 1) as in any ATR program, it provides synthetic data sets for algorithm evaluation, and 2) *simulation provides the heart of the ATR algorithm itself.* The likelihood is combined with a prior distribution defined over the set of possible scenes to form a posterior distribution. Since the number of objects in the scene (the model order) is not known in advance, we must define a single posterior probability across all of the model subspaces.

In the realm of FLIR and visual images, our maxim of *pattern recognition = pattern synthesis* may be formulated as *computer vision = computer graphics*, an idea championed by Gagalowicz[9] and employed by Talluri and Aggarwal for autonomous navigation[10].

1.2 Inference via Jump-Diffusions

Our applications possess discrete and continuous aspects. The sensor will be presented with an unknown number of targets. In addition, the targets themselves will likely be members of some small set of vehicles. These parameters are discrete in nature. The positions and orientations of targets are inherently continuous in nature.

We have built the logical and computational engines of our deduction algorithms around jump-diffusion processes which provide the dynamic flexibility to accomodate higher and lower complexity scenes [3, 11, 12]. *Jump-diffusions* are inherently discrete and continuous in the nature of their search, and therefore accommodate the very different continuous and discrete nature of image understanding. The *jumps* deal with changes of target type and number and the *diffusions* [13] accommodate the continuous parameters. Technically, jump-diffusion algorithms permit sampling from complex posterior distributions which would otherwise be difficult or impossible to simulate directly.

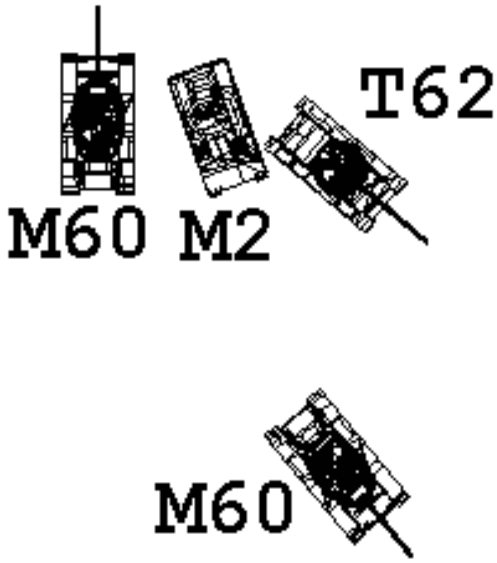

Figure 1: Top-down view of a configuration of targets.

2 THE BAYESIAN MODELS

Figure 1 illustrates a top-down representation of a particular configuration of ground-based targets. Sensors such as imaging laser radars and visual and infrared cameras observe the scene through the effects of *obscuration* and *perspective projection*, in which a point (x, y, z) in 3-D space is projected onto the 2-D detector according to $(x, y, z) \mapsto (x/z, y/z)$, as shown in Figure 2. This creates the vanishing point effect in which objects which are further away from the sensor appear closer to the center of the detector. Objects will appear skewed in different ways depending on where they appear in the image plane.

2.1 Infrared (FLIR) Model

FLIR cameras passively sense objects via the infrared radiation they emit or reflect. In the bands we are concerned with, particularly the 8-12 micron band, emitted radiation is the dominant effect. The radiation emitted depends upon the thermodynamic state of the object and its emissivity properties. Atmospheric absorption attenuates the radiation reaching the sensor. We will ignore

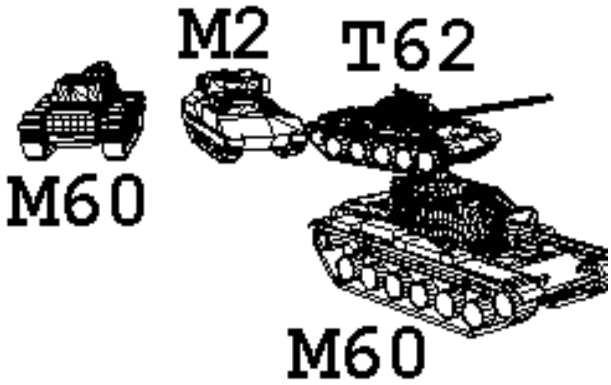

Figure 2: Wireframes of targets viewed under perspective projection and obscuration.

such absorption effects here, although they could easily be incorporated in the model.

For now, we will assume the Earth is a flat surface of constant known intensity on the x-z plane extending infinitely in all directions. We will also assume that the sky radiates a constant known intensity. We plan to relax these assumptions in future work.

We currently assume that target facets radiate known intensities. The intensities may be determined from measured data [14], simulation (such as PRISM [15] or GTSIG [16]), or a combination of the two [17]. In these simulations we employ radiances predicated by the PRISM (Physically Reasonable Infrared Signature Model) software [15] developed by Michigan Technological University's Keweenaw Research Center (data courtesy Dr. A. Curran, Michigan Tech/KRC) under the direction of TACOM. Wireframe models and associated radiance images of some orthogonal "draftsman" views of the M2, the M60, and the T62 are shown in Figure 3.

Unfortunately, real FLIR sensors are subject to various sources of error. We will invoke the CCD camera model of Snyder, Hammoud, and White [18]. The camera introduces blurring according to

$$\mu(\mathbf{y}) = \sum_{\mathbf{p}\in\mathcal{P}} q(\mathbf{y}|\mathbf{p})\lambda^{IR}(\mathbf{p}), \qquad (1)$$

where $\lambda^{IR}(\mathbf{p})$ is the ideal observed intensity and $q(\mathbf{y}|\mathbf{p})$ is the camera point spread function, normalized so that $\sum_{\mathbf{y}\in\mathcal{Y}} q(\mathbf{y}|\mathbf{p}) = 1$. For simplicity, we disregard background counts, readout noise, nonuniform response, and wavelength dependency in the camera, but these distor-

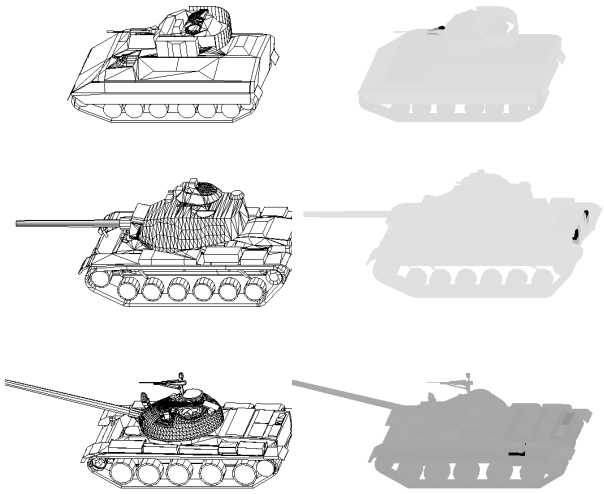

Figure 3: Orthogonal views of faceted models of an M2 (top), an M60 (middle), and a T62 (right). Wireframes are shown on the left, associated PRISM radiances on the right. Courtesy Dr. A. Curran, Keweenaw Research Center, Michigan Technological University.

tions could be accommodated readily.

Figure 4 shows an ideal infrared scene λ^{IR} corresponding to Figure 2. We have embedded the PRISM models in a real infrared image. Here, the real infrared background does not match the perspective of the object models; the real image is only intended to provide a reasonable desert background texture. Figure 5 shows the corresponding μ, this ideal infrared scene λ^{IR} blurred with a Gaussian point-spread function q.

The data $D^{IR}(\mathbf{y})$ collected by a CCD camera is Poisson distributed with mean $\mu(\mathbf{y})$. A sample of Figure 4 with Poisson noise is shown in Figure 6. The Poisson loglikelihood of the data D^{IR} given λ^{IR} is

$$L^{IR}(D^{IR}|\lambda^{IR}) = -\sum_{\mathbf{y}\in\mathcal{Y}} \mu(\mathbf{y}) + \sum_{\mathbf{y}\in\mathcal{Y}} \ln[\mu(\mathbf{y})]D^{IR}(\mathbf{y}). \quad (2)$$

Given an estimated configuration x and a series of images D^{IR}_{κ} collected at discrete times $\kappa = 0 \ldots \kappa_T$, where κ_T is the current time, we can write

$$L^{IR}_{\kappa_T}(D^{IR}|c) = \sum_{\kappa=0}^{\kappa_T} L^{IR}(D^{IR}_{\kappa}|render^{IR}(x)), \qquad (3)$$

where $render^{IR}(x)$ represents the operation of rendering, via perspective projection and obscuration, the radiant intensities of the objects in the configuration and the

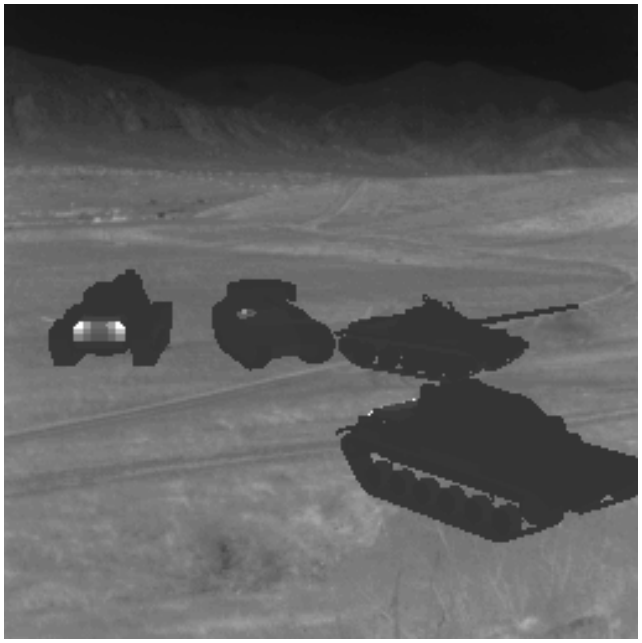

Figure 4: Ideal infrared scene without point-spread.

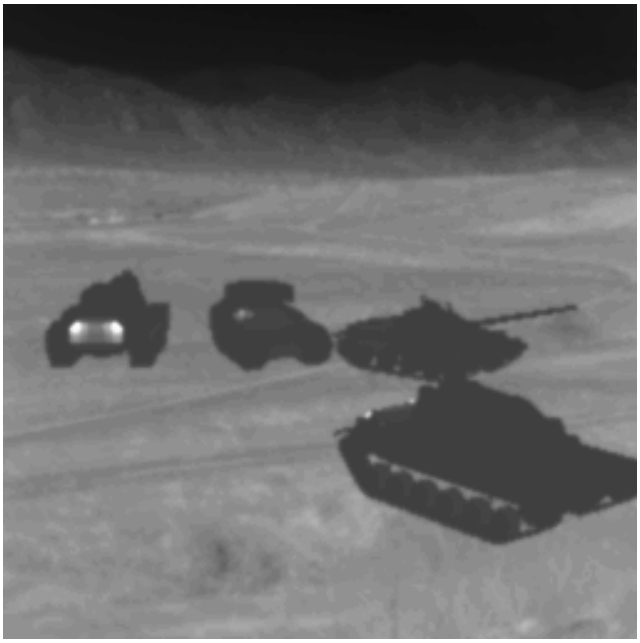

Figure 5: Ideal infrared scene as viewed through a with a Gaussian point-spread function.

background onto the image plane. Note that this rendering process (which we have implemented on the Silicon Graphics) may be quite intricate; thus, the loglikelihood is a highly nonlinear, extremely complicated function of the configuration parameters.

Real FLIR images will also contain manufacturing artifacts such as dead and saturated pixels. We have randomly placed such artifacts uniformly across the image in Figure 6 to make Figure 7. This is the data that our algorithm processes in Section 4. Although the likelihood model used here does not explicitly incorporate these artifacts, they have little effect on the performance of the algorithm.

2.2 Laser Radar (LADAR) Model

Here we will explore a model for laser radar range data. Intensity and Doppler information, if available, can be incorporated similarly.

Let $\lambda^{LR}(\mathbf{y})$ be the true distance from the sensor to the scene at pixel $\mathbf{y}$. We will employ Shapiro's model for laser radar range images [19, 20, 21], with a few changes to suit our purposes. In particular, we will explicitly incorporate the ambiguity inherent in the range measurements, so the measurements are more accurately characterized as taking values on the torus rather than the real line. Although a wrapped Gaussian or Von Mises density would be more appropriate for toroidal data, we will employ Shapiro's original Gaussian density as a reasonable approximation. The loglikelihood of collecting range data D^{LR} given true range λ^{LR} is then

$$L^{IR}(D^{LR}|\lambda^{LR}) = \sum_{\mathbf{y}\in\mathcal{Y}} \ln\{\frac{Pr_A(\mathbf{y})}{\Delta R} + [1 - Pr_A(\mathbf{y})] \times \quad (4)$$

$$\frac{\exp[-(D^{LR}(\mathbf{y}) - [\lambda^{LR}(\mathbf{y}) \bmod \Delta R])^2/(2\delta(\mathbf{y})^2)]}{\sqrt{2\pi\delta(\mathbf{y})^2}}\} \quad (5)$$

where ΔR is the extent of the range uncertainty interval and $\delta(\mathbf{y})$ and $\mathrm{Pr}_A(\mathbf{y})$ are the local range accuracy and probability of anomalous measurement for pixel $\mathbf{y}$ given by $\delta(\mathbf{y}) = R_{res}/\sqrt{CNR(\mathbf{y})}$ and $Pr_A(\mathbf{y}) = [ln(N) - 1/N + 0.577]/CNR(\mathbf{y})$, where $N = \Delta R/R_{res}$, R_{res} is the range resolution, and CNR is the carrier-to-noise ratio taken to be $CNR(\mathbf{y}) = \Xi \exp\left[-2\alpha\lambda^{LR}(\mathbf{y})\right] / \left[\lambda^{LR}(\mathbf{y})\right]^2$, where α is the atmospheric extinction coefficient and Ξ is a constant derived from the properties of the laser radar. Notice that the probability of anomaly $Pr_A(\mathbf{y})$ and the local range accuracy $\delta(\mathbf{y})$ *increase with hypothesized distance* $\lambda^{LR}(\mathbf{y})$.

Figure 8 presents an example of a noiseless range image (with ambiguity) corresponding to Figure 2. A sample of this image corrupted with anomolous pixels and range-dependent measurement error is shown in Figure 8.

Given an estimated configuration x and a series of images D^{LR}_{κ} collected at discrete times $\kappa = 0 \ldots \kappa_T$, where κ_T

Figure 6: A FLIR image corrupted by Poisson noise.

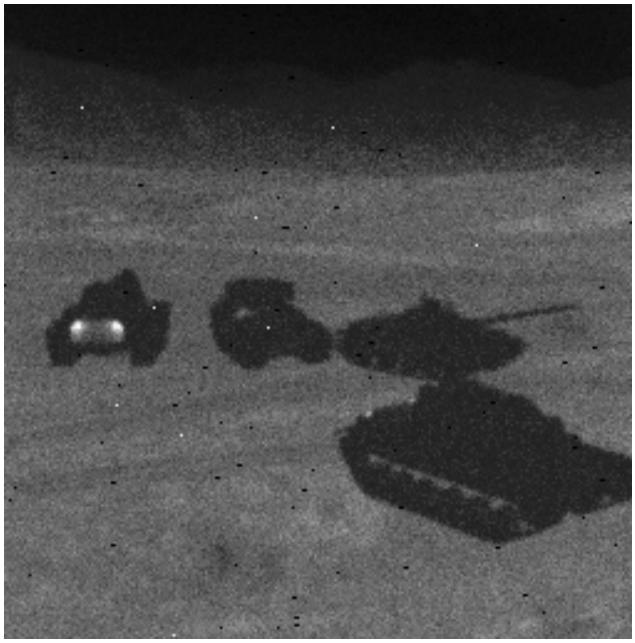

Figure 7: FLIR image with Poisson noise and uniformly distributed dead and saturated pixels.

is the current time, we can write

$$L^{LR}_{\kappa_T}(D^{LR}|c) = \sum_{\kappa=0}^{\kappa_T} L^{LR}(D^{LR}_{\kappa}|render^{LR}(x)), \quad (6)$$

where $render^{LR}(x)$ represents the operation of rendering, via perspective projection and obscuration, the range to elements of the scene.

Many computer graphics engines, including the Silicon Graphics hardware, account for obscuration with a *z-buffer algorithm.* As object pixels are rendered, their distance is stored in a pixel-registered z-buffer. New pixels are only written to the rendered image if their distance is less than what is currently stored in the z-buffer. After the scene is fully rendered, the final contents of the z-buffer provide ranges as a by-product of the rendering algorithm. Thus, *in simulating infrared images* λ^{IR} *we can essentially get simulated range images* λ^{LR} *"for free."*

2.3 Posterior Distribution

To fuse data from different modalities, we simply add their loglikelihoods, e.g. $L = L^{IR} + L^{LR}$.

For a prior, we assume a uniform distribution on target types and orientations and a uniform distribution with finite support on target positions. Ideally, the prior should incorporate the fact that two targets cannot occupy the same physical space. However, we have currently found explicit implementation of such a prior to be unnecessary. When hypothesizing new targets, we just make sure the new target does not fall too close to an existing target.

The likelihood and prior combine to form a posterior density in Gibbs form

$$\pi_{\kappa_T}(x|D) \propto \exp[H_{\kappa_T}(x|D)] \quad (7)$$

where $P_{\kappa_T}(x)$ is the logprior and $H_{\kappa_T}(x|D) = L_{\kappa_T}(D|x) + P_{\kappa_T}(x)$ is the logposterior. Note that the posterior distribution changes with time as we collect more data. Since computational and storage requirements grow rapidly as we collect more and more data, in practice we will only retain a few of the most recently collected data frames in memory.

We sample from (7) by simulating a random process as described in the next section.

3 INFERENCE ALGORITHM

3.1 Diffusion Process

Since the diffusion process cannot change the number of targets or target types, we will have a family of diffusion processes to jump between. Each diffusion process in this

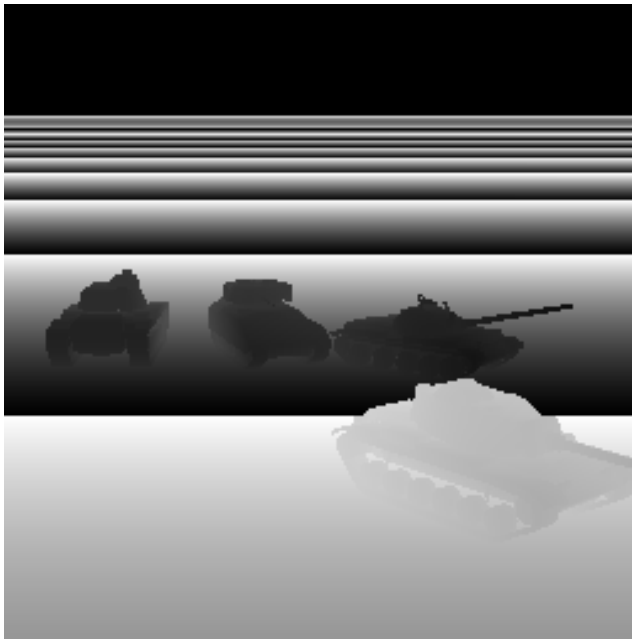

Figure 8: Noise-free LADAR range image with range ambiguity.

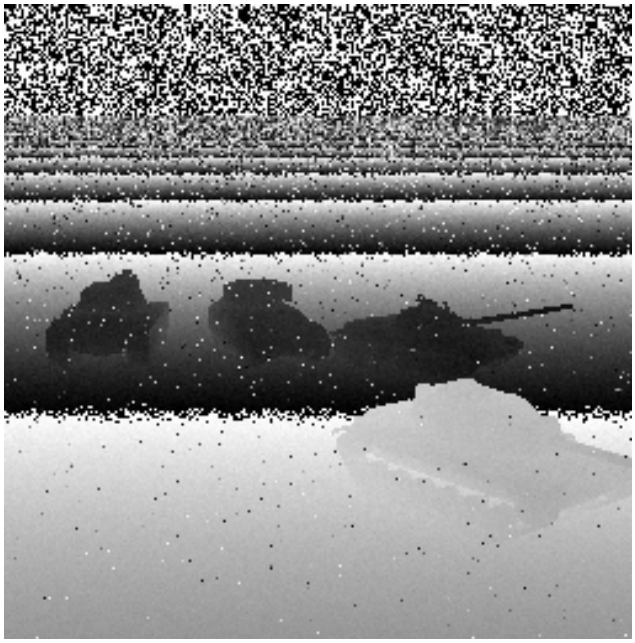

Figure 9: Sample LADAR range image with range ambiguity, anomolous pixels, and range-dependent measurement errors.

family is a stochastic gradient ascent which samples from an associated posterior distribution. The different diffusion processes correspond to different numbers of targets and different target types. Consider the composite parameter vector for an N-target configuration with fixed target classes at time κ_T

$$X_N = (x(1), x(2), \ldots, x(N)) \in \mathcal{X}_N. \tag{8}$$

For the ground based targets of interest here, we represent the targets with a position on the plane and an orientation about the y-axis, so let $\mathcal{X}_N = [\Re^2 \times [0, 2\pi)]^N$.

Our approach is to formulate a diffusion process $X_N(\tau)$ which has the property that the distribution of $X_N(\tau)$ converges in variation norm to $\pi(X_N|D) \propto \exp H(X_N|D)$, the posterior distribution for the parameter space space $\mathcal{X}_N$. Using a discretization with a sufficiently small step size, we simulate the diffusion process defined by the Langevian stochastic differential equation

$$dX_N(\tau) = \nabla_{X_N} H(X_N(\tau)|D)d\tau + \sqrt{2}dW_N(\tau), \tag{9}$$

where $W_N(\tau)$ is a Weiner process in $\mathcal{X}_N$, and $H(X_N|D)$ is the logposterior associated with the parameter vector X_N. For the orientation parameter, additions are taken modulo 2π. The "algorithmic time" τ should not be confused with the real-world time κ over which the data is gathered.

3.2 Jump Process

Jumps allow the inference algorithm to visit subspaces with different numbers of targets and different target types. This accommodates the discrete nature of the problem. We employ three types of simples moves: *births*, to hypothesize new targets; *deaths*, to remove target hypotheses not well supported by the data; and *metamorphs*, to change hypothesized target type.

A variety of jump-diffusion processes may be formulated, all of which will result in the desired invariant measure. The different schemes correspond to different choices of the *jump intensity* $q(x, dy)$. Let $\mathcal{T}^1(x)$ be the set of states which may be reached from state x in one jump move. Here, $\mathcal{T}^1(x) = \mathcal{T}^1_b(x) \cup \mathcal{T}^1_d(x) \cup \mathcal{T}^1_m(x)$, where the $T^1_b(x)$, $T^1_d(x)$, $T^1_m(x)$ represent the set of states which may be reached from x via a birth, a death, and a metamorph. Similary, define $\mathcal{T}^{-1}(x)$ to be the set of states which may reach x in one jump move.

The jumps occur at exponentially distributed times. Given a set of times w_1, w_2, ..., independent and exponentially distributed, the jump times τ_1, τ_2, ... are given by

$$\tau_i = \inf\{\tau : \int_{\tau_{i-1}}^{\tau} q(X(\tau'))d\tau' \geq w_i\}, \tag{10}$$

where $q(x) = \int_{\mathcal{T}^1(x)} q(x, dy)$. Between jumps, the process satisfies the stochastic differential equation (9) appropriate for that subspace. At each jump, the process moves from state x to a new state y according to the *jump transition probability measure* $Q(x, dy) = q(x, dy)/q(x)$.

In order to achieve the desired ergodic property, we choose the jump intensities so that

1. The jump moves are reversible, i.e., $\mathcal{T}^1(x) = \mathcal{T}^{-1}(x)$,
2. The family of jump moves are rich enough to permit any subspace to be reached from any other disconnected subspace in a finite number of jump moves,
3. $q(x)$ and $Q(x, dy)$ are bounded continuous functions, and
4. The jump intensities satisfy the *detailed balance condition*

$$q(x)\pi(x)dx = \int_{\mathcal{T}^{-1}(x)} q(y, dx)\pi(y)dy. \qquad (11)$$

Then, according to Theorems 1 and 2 from [3], the jump-diffusion process described above possesses the desired unique invariant measure. The exact hypotheses required for convergence are quite intricate and may be found in [22, 23, 3].

We will choose a jumping scheme analogous to the Metropolis-Hastings sampling algorithm [24, 25, 26]. At exponentially distributed times, with $fixed$ mean λ_{jump}, we draw a candidate x_{prop} from a *proposal density* $r(x_{old}, x_{prop})$ and compute the *acceptance probablity*

$$\alpha(x_{old}, x_{prop}) = \min\{\frac{\pi(x_{prop})r(x_{prop}, x_{old})}{\pi(x_{old})r(x_{old}, x_{prop})}, 1\}. \qquad (12)$$

The proposal is accepted with probability $\alpha(x_{old}, x_{prop})$ and rejected with probability $1 - \alpha(x_{old}, x_{prop})$. A wide variety of proposal densities may be used; we merely require that $r(x_{old}, x_{prop}) > 0$ for $x_{prop} \in \mathcal{T}^1(x_{old})$ and $r(x_{old}, x_{prop}) = 0$ for $x_{prop} \notin \mathcal{T}^1(x_{old})$.

This scheme corresponds to choosing the jump intensity

$$q(x, dy) = \min\{\frac{\pi(y)r(y, x)}{\pi(x)r(x, y)}, 1\}r(x, y)dy. \qquad (13)$$

In this study, we choose a proposal density which proposes a *birth*, *metamorph*, or *death* move according to the prior on the number of targets and draws the proposal from the posterior density over the space which can be reached via the proposed move type. Further details are given in [4].

4 EXAMPLES

4.1 FLIR Data

We have implemented a jump-diffusion algorithm for FLIR on a Silicon Graphics Onyx/Reality Engine. Implementation details may be found in [4, 6]. Figure 10 shows interesting states of a sample path of the process running on the data shown in Figure 7.

Since we started the process with an empty configuration, the algorithm tries a birth on the first iteration. The M60 on the right appears larger than the other targets since it is closer to the sensor. The algorithm finds it first since it can "explain" the largest amount of data pixels with it. In iteration 3, it mistakes the T62 for an M60. It does this since it hasn't yet found the adjacent M2 and is trying to explain some of the M2's pixels using the barrel of the M60. This demonstrates the importance of moves which allow changes of type. In iteration 24, the algorithm finds the M2, but the hypothesis is facing the wrong direction. While the diffusions may refine orientation estimates, they are impractical for making large orientation changes, suggesting the necessity of a jump move for making such drastic changes in orientation. Notice the diffusions have found the correct placement of the M60. The remaining M60 is found in iteration 32. The algorithm continues to propose birth moves which are rejected since the data does not support a fifth target.

In iteration 34, the barrel of the incorrectly-guessed M60 is no longer needed to explain the M2 pixels, so a metamorph move swings the hypothesis around, but still incorrectly supposes it to be an M60. It is flipped back the other direction and incorrectly supposed to be an M2 in iteration 68.

Between iterations 68 and 87, the diffusions pull the incorrectly-hypothesized M2 closer to the correct position, so a metamorph move in iteration 88 correctly changes its type to a T62. The correct orientation of the true M2 is found in iteration 103. The configuration (all of the types, positions, and orientations) has been correctly deduced by iteration 117. All throughout the inference, the algorithm proposes death moves which are rejected.

4.2 LADAR Range Data

We have recently tried modifying the algorithm described above to incorporate the LADAR range model instead of the FLIR model. Interesting snapshots of a sample path

analyzing the data in Figure 9 are shown in Figure 11. Notice that, in this preliminary experiment, the algorithm incorrectly estimates the orientation of the M2.

5 DIRECTIONS FOR FUTURE WORK

Throughout this study, we have assumed that target facets radiate known intensities. In general, we can not expect facet intensities to be exactly known, since the target may radiate a range of intensities depending on operating and environmental conditions. Traditional approaches to ATR attempt to extract features which are invariant to such changes in intensity. In our context, we would summarize the target's thermodynamic state with a parsimonious set of variables. In one view, these are nuisance parameters which should be averaged out. From our point of view, these parameters might provide useful information about the object (for instance, whether a tank has been idling or running at top speed all day.)

Land-based vehicles are just a small subset of the types of objects a FLIR sensor will encounter. We intend to expand our framework to incorporate more complex man-made objects such as buildings, roads, and runways, as well as natural ones such as lakes. Although in one sense these are nuisance parameters, in another sense they could help identify the man-made structures we are interested in, because we could enrich the knowledge representations to encapsulate such notions as "the jeep is in the lake" and "the submarine is on the runway." The prior could aid recognition by realizing that neither of those two statements is a likely possibility. Incorporating hills, mountains, valleys, and other such geographical structures will involve relaxing the assumption that the earth is a flat surface.

Compared to the emissive characteristics of man-made structures, the emissive characteristics of natural backgrounds [27] are not well understood [28]. More complex models for the ground, perhaps incorporating Markov random field texture models, could be employed. Markov random fields have proven beneficial [29, 30, 31] for texture analysis in the segmentation of electron micrographs [23, 3]. In addition to algorithms for model-based image segmentation, algorithms have been developed which postulate appropriate models from training data using Rissanen's minimum description length criterion [32, 33, 34]. The analysis of textures in infrared images will be especially challenging since the apparent textures change with distance from the detector.

6 ACKNOWLEDGEMENTS

This work was supported by ONR N00014-92-J1418, ONR/AASERT N00014-94-1-1135, ARO DAAL03-92-G-0141, and ARO/AASERT DAAH04-94-G-0209.

References

[1] U. Grenander. *General Pattern Theory.* Oxford University Press, 1993.

[2] D. Mumford. Pattern theory: a unifying perspective. In *Proceedings 1st European Congress of Mathematics.* Birkhauser, 1994.

[3] U. Grenander and M. I. Miller. Representations of knowledge in complex systems. *Journal of the Royal Statistical Society B*, 56(3):549–603, 1994.

[4] A.D. Lanterman. Jump-diffusion algorithms for the automated understanding of forward-looking infrared scenes. Master's thesis, Washington University, St. Louis, MO, May 1995.

[5] A.D. Lanterman, M.I. Miller, D.L. Snyder, and W.J. Miceli. Jump-diffusion processes for the automated understanding of flir scenes. In F.A. Sadjadi, editor, *Automatic Object Recognition IV*, volume 2234, pages 416–427, Orlando, FL, April 1994. SPIE.

[6] A.D. Lanterman, M.I. Miller, and D.L. Snyder. Implementation of jump-diffusion processes for understanding flir scenes. In F.A. Sadjadi, editor, *Automatic Object Recognition V*, volume 2485, pages 309–320, Orlando, FL, April 1995. SPIE.

[7] M.K. Hamilton and T.A. Kipp. Model-based multisensor fusion. In Avtar Singh, editor, *Conference Record of the Twenty-Seventh Asilomar Conference on Signals, Systems and Computers*, pages 283–289, Los Alamitos, California, November 1993. IEEE Computer Society Press.

[8] P. Bhattacharya. Aspect angle estimation of targets in forward-looking infrared imagings using the model-based vision approach. *Optical Engineering*, 33(10):3334–3341, October 1994.

[9] A. Gagalowicz. Collaboration between computer graphics and computer vision. In *Proc. 4th ICCV*, pages 733–737, December 1990.

[10] R. Talluri and J.K. Aggarwal. Image/map correspondence for mobile robot self-location using computer graphics. *IEEE Trans. Pattern Anal. Machine Int.*, 15:597–601, June 1993.

[11] M.I. Miller, A. Srivastava, and U. Grenander. Conditional-mean estimation via jump-diffusion processes in multiple target tracking/recognition. *IEEE Transactions on Signal Processing*, accepted for publication, November 1994.

[12] A. Srivastava, M.I. Miller, and U. Grenander. Multiple target direction of arrival tracking. *IEEE Transactions on Signal Processing*, 43:1282–1285, May 1995.

[13] S. Geman and C.-R. Hwang. Diffusions for global optimization. *SIAM J. Control and Optimization*, 24:1031–1043, 1987.

[14] C.E. Lucius. Targeting systems characterization facility. In *Thermal Imaging*, pages 40–46. SPIE 636, 1986.

[15] *Prism 3.1 User's Manual.* Keweenaw Research Center, Michigan Technological University, 1987.

[16] J.M. Catchart and Jr. A.D. Sheffer. Generation and application of high-resolution infrared computer imagery. *Optical Engineering*, 30(11):1745–1755, November 1991.

[17] W.R. Owens. Data-based methodology for infrared signature projection. In *Thermal Imaging*, pages 96–99. SPIE 636, 1986.

[18] D.L. Snyder, A.M. Hammoud, and R.L. White. Image recovery from data acquired with a charge-coupled-device camera. *Journal of the Optical Society of America A*, 10(5):1014–1023, May 1993.

[19] J. Shapiro, B.A. Capron, and R.C. Harney. Imaging and target detection with a heterodyne-reception optical radar. *Applied Optics*, 20, No.19:3292–3313, 1981.

[20] Jr. T. J. Green and J. H. Shapiro. Detecting objects in 3d laser radar range images. *Opt. Eng.*, 33:865–873, March 1994.

[21] Jr. T. J. Green and J. H. Shapiro. Maximum-likelihood laser radar range profiling with the expectation-maximization algorithm. *Opt. Eng.*, 31:2343–2354, 1992.

[22] Y. Amit, U. Grenander, and M.I. Miller. Ergodic properties of jump-diffusion processes. *Annals of Applied Probability*, submitted January 1993.

[23] U. Grenander and M. I. Miller. Jump-diffusion processes for abduction and recognition of biological shapes. *Monograph of the Electronic Signals and Systems Research Laboratory*, 1991.

[24] W. K. Hastings. Monte carlo sampling methods using markov chains, and their applications. *Biometrika*, 57,2:97–109, 1970.

[25] P.J. Green. Monte carlo methods: An overview. In *invited contribution to Proceedings of the IMA Conference on Complex Stochastic Systems and Engineering*, 1993.

[26] P.J. Green. Markov chain monte carlo in image analysis. In D. Spiegelhalter W. Gilks, S. Richardson, editor, *Practical Markov Chain Monte Carlo*. Chapman and Hall, to appear 1995.

[27] N. Ben-Yosef, K. Wilner, I. Fuchs, S. Simhony, and M. Abitbol. Natural terrain infrared radiance statistics: Daily variation. *Applied Optics*, 24, No. 9:4167–4174, December 1985.

[28] P. Jacobs. Review of the technology and research in the area of infrared signatures of targets and backgrounds. In *Characterization, Propagation, and Simulation of Infrared Scenes*, pages 80–94. SPIE 1311.

[29] J. Besag and P. J. Green. Spatial statistics and bayesian computation. *J. Royal Statistical Society B*, 55(1):25–38, 1993.

[30] J. Besag. On the statistical analysis of dirty pictures. *J. Royal Statistical Society B*, 48(3):259–302, 1986.

[31] J. Besag. Spatial interaction and statistical analysis of lattice systems (with discussion). *J. Royal Statist. Soc.*, series B, vol. 36:192–326, 1974.

[32] K. R. Smith. A bayesian approach incorporating stochastic complexity for learning regular grammar models and image models: Application to segmenting biomedical images. Master's thesis, Washington University, St. Louis, MO, December 1990.

[33] K.R. Smith and M.I. Miller. *Bayesian Inference of Regular Grammar and Markov Source Models*, pages 388–398. Morgan-Kaufmann, Inc. in Palo Alto, 1990.

[34] K.R. Smith and M.I. Miller. A bayesian approach incorporating Rissanen complexity for learning Markov random field texture models. *Proceedings of the Intl. Conference on Acoustics, Speech, and Signal Processing*, 4:2317–2320, April 1990.

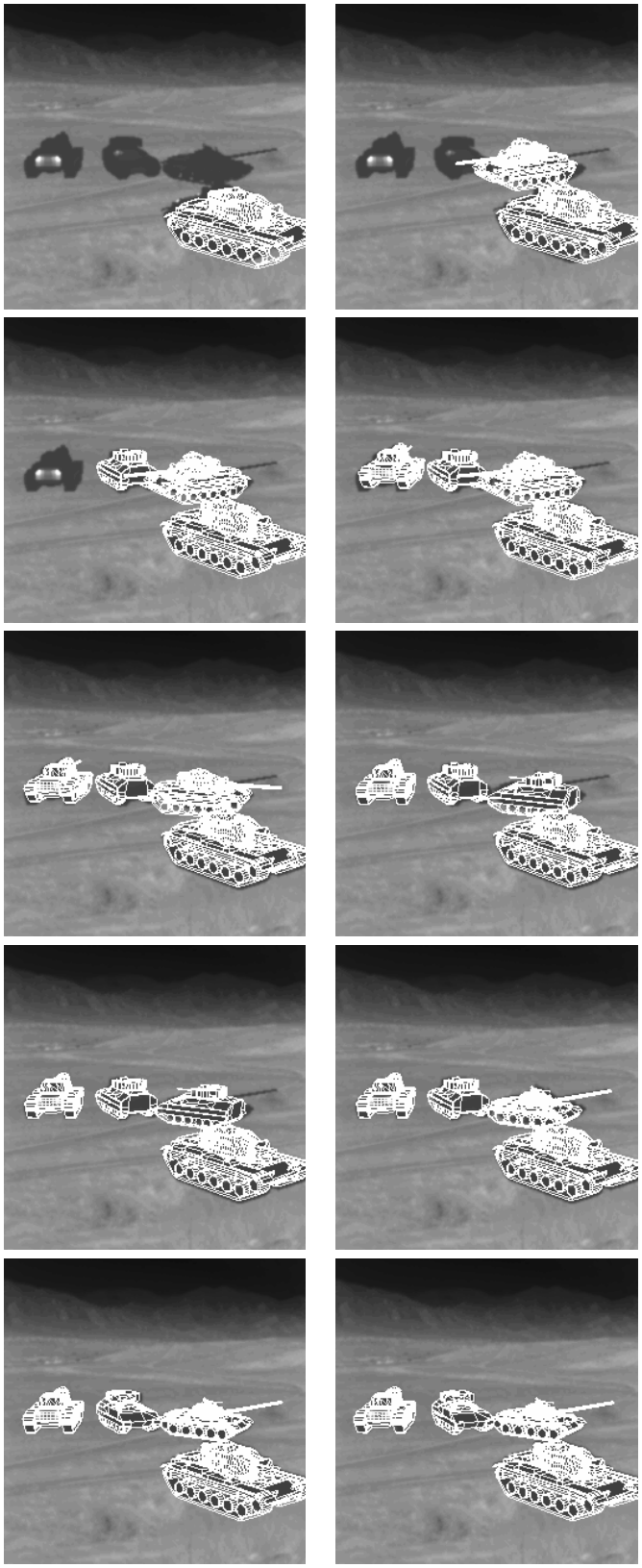

Figure 10: Iterations 1, 3, 24, 32, 34, 68, 87, 88, 103, and 117 of a jump-diffusion process for FLIR data.

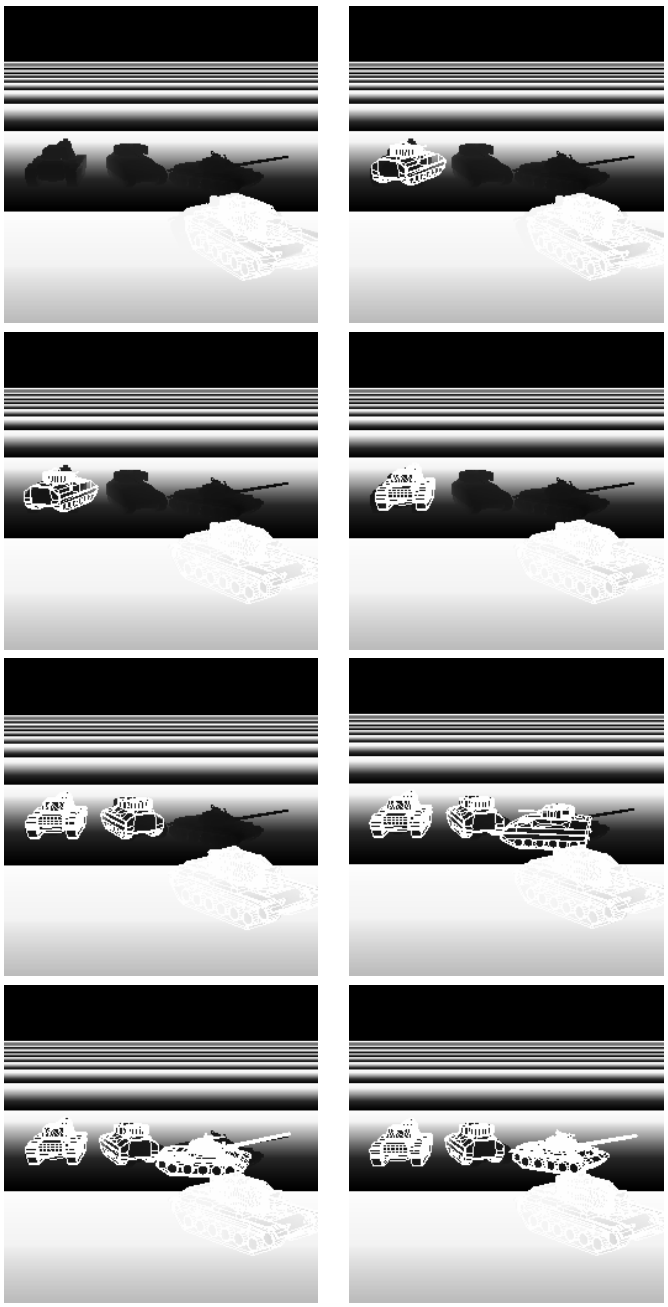

Figure 11: Iterations 1, 3, 11, 12, 24, 32, 38, and 130 of a jump-diffusion process for LADAR range data.